The critical effect of rail vertical phase response in railway curve squeal generation

Van-Vuong Lai, Olivier Chiello, Jean-François Brunel, Philippe Dufrenoy

▶ **To cite this version:**

Van-Vuong Lai, Olivier Chiello, Jean-François Brunel, Philippe Dufrenoy. The critical effect of rail vertical phase response in railway curve squeal generation. International Journal of Mechanical Sciences, 2020, 167, 23 p. 10.1016/j.ijmecsci.2019.105281 . hal-02362786v1

HAL Id: hal-02362786

https://hal.science/hal-02362786v1

Submitted on 21 Dec 2021 (v1), last revised 18 Mar 2022 (v2)

HAL is a multi-disciplinary open access archive for the deposit and dissemination of scientific research documents, whether they are published or not. The documents may come from teaching and research institutions in France or abroad, or from public or private research centers.

L'archive ouverte pluridisciplinaire **HAL**, est destinée au dépôt et à la diffusion de documents scientifiques de niveau recherche, publiés ou non, émanant des établissements d'enseignement et de recherche français ou étrangers, des laboratoires publics ou privés.

Distributed under a Creative Commons Attribution - NonCommercial 4.0 International License

Version of Record: https://www.sciencedirect.com/science/article/pii/S0020740319316157
Manuscript_9f4e530b47109cc505b2e9aba3e4b94f

The critical effect of rail vertical phase response in railway curve squeal generation

Van-Vuong Lai[b,*], Olivier Chiello[a], Jean-François Brunel[b], Philippe Dufrénoy[b]

[a] *Univ Lyon, IFSTTAR, CEREMA, UMRAE, F-69675, Lyon, France*
[b] *Univ. Lille, CNRS, Centrale Lille, FRE 2016 - LaMcube - Laboratoire de Mécanique Multiphysique Multiéchelle, F-59000, Lille, France*

Abstract

Squeal of rail-bound vehicles emitted in tight curves is characterized by high sound pressure levels at pure medium and high frequencies. Many models have been proposed in the literature to explain the occurrence of this noise with different instability mechanisms: negative damping due to falling friction or instability with a constant friction coefficient. The aim of the paper is to contribute to the understanding of the instability mechanisms in the case of a constant friction coefficient. A stability analysis of the wheel/rail contact dynamics in curve is performed by using an equivalent point contact model combined with wheel and rail modal bases. Results show that even with an assumption of a constant Coulomb friction coefficient, two types of instabilities may occur in the wheel/rail system: classical mode coupling and instabilities due to negative damping added to a single wheel mode when the track dynamical behavior, especially in the vertical direction, is included. For this second type of instabilities, an 1-degree of freedom model can be formulated. By using this model, it is found that the equivalent damper behavior of the infinite track is the origin of these instabilities.

Keywords: Curve squeal, Wheel/Rail contact, Stability analysis, Instability mechanism.

1. Introduction

When a railway vehicle negotiates a tight curve, a strong noise called curve squeal may be emitted. The sound pressure levels can reach 130 dB close to the wheel, and up to 110 dB at 7.5 m from the track center [1]. It has been observed by Eadie *et al.* that squeal due to high lateral slip of the wheel on the rail-head tends to occur in the range of 1000 − 5000 Hz, whereas squeal noise due to wheel flange contact shows spectral characteristics primarily in the range of 5000 − 10000 Hz [2]. The predominating part of squeal energy is concentrated in one or several pure tone frequencies [3]. Experimental observations (cf. for instance [4]) show that curve squeal is strongly influenced by the local kinematic parameters at wheel/rail contact, the friction at contact interface and the wheel vibro-acoustic characteristics. The measurements described by Rudd [5], Vincent *et al.* [3], Koch *et .al* [4] and Glocker *et .al* [6] show that the wheel radiates at frequencies close to its natural frequencies. In addition, the highest noise level is often radiated by the inner leading wheel. However, squeal is occasionally observed on the outer wheel [6].

Although longitudinal wheel slip and wheel flange contact have originally been cited as a cause of curve squeal, they have been discredited as a main energy input in several works [3, 5, 7]. Most of mechanisms proposed in the literature put forward the high lateral slip of the wheel on the rail-head as the main cause of curve squeal. Indeed, in tight curves, a steady lateral sliding motion is imposed to the wheel due to the misalignment between wheel and rail (angle of attack or yaw angle). A widespread assumption is that the friction forces generated by the sliding motion may lead to structural instability and self-sustained vibration of the wheel/rail system. Like brake squeal, curve squeal is also considered as a kind of friction-induced vibrations. Two instability mechanisms have been proposed to explain the origin of friction-induced vibrations: falling friction and mode coupling. Many studies [8–10] dealt with the

*Corresponding author
Email address: vanvuong.lai1990@gmail.com (Van-Vuong Lai)

© 2019 published by Elsevier. This manuscript is made available under the CC BY NC user license
https://creativecommons.org/licenses/by-nc/4.0/

falling friction mechanism. A falling slope in the velocity-dependent friction law can be mathematically expressed as a negative damping leading to an unstable behavior. The notion of mode coupling was notably introduced by Oden and Martins in [11] following the observation of a coupling between the normal and tangential directions carried out in [12, 13]. Many studies [14–16] proposed 2-degree of freedom (DOF) models to highlight this mechanism. Mathematically, this is the non-symmetric stiffness matrix due to friction which leads to instability. Without the system damping, this instability is characterized by a perfect coalescence between the frequencies of an unstable complex mode and another stable complex mode when the friction coefficient reaches a critical value.

Models proposed in [5, 17–25] show that a falling friction law can generate instabilities of wheel/rail contact. The unstable frequencies found are generally close to axial wheel modes with 0 nodal circle. However, Brunel [26] obtained squeal even if the friction law is positive. It is concluded that squeal is due to the coupling of the normal and lateral dynamics by the Poisson ratio of the wheel material (sprag-slip phenomena). The consideration of mode coupling instability in curve squeal models is relatively recent. Although such a mechanism may occur with a constant friction coefficient, it needs to take into account the vertical dynamics of the system. In the case of constant friction coefficient and rigid rail, Glocker *et al.* [6] found that mode coupling occurs with a number of wheel modes with closely spaced natural frequencies: one axial mode with zero nodal circles and two radial modes of the wheel. Ding *et al.* [27] also demonstrated that a mode-coupling instability can occur and there is a slight gap between the squealing frequency and the natural frequency of the wheel modes. In the case of constant friction coefficient and flexible rail, Pieringer [28], Zenzerovic [29, 30] showed that curve squeal can occur due to coupling of the normal and lateral dynamics of a single wheel mode. Finally, Ding *et al.* [24] found that the dynamic rail plays an important role by suddenly changing the stability of the system in the case of constant friction coefficient. If the rail dynamic is not included, the unstable frequencies seem to be caused by the coupling of wheel modes. Otherwise, almost unstable frequencies get close to axial wheel modes with 0 nodal circle. Ding *et al.* concluded that this is due to the coupling of the normal and lateral component of the single wheel mode when the flexibility of normal contact is changed by the rail dynamics.

From the results of existing curve squeal models, the instability mechanisms are still controversial. In the case of friction coefficient decreasing with creep velocities, the phenomena are rather straightforward. Instability is caused by the negative damping introduced by the slope of creep/friction curve for large creepages. The results of the models correspond well to experimental observations such as instabilities of axial modes with zero nodal circle and creep/slip limit cycles. However, the slope of the friction coefficient is not really proved in experimental terms. Experimentally, it is difficult to measure the dynamic creep quantities (especially contact forces) and the dynamic curve is not accessible. So one may wonder whether the addition of this slope is artificial but not a physical means to bring out the instability. In the case of constant friction coefficient and provided that the rail dynamics is taken into account, one can also find results consistent with experimental observations such as instabilities of axial modes with zero nodal circle and creep/slip limit cycles [24, 28–30]. However, the mechanisms behind this instability are not clear. To study this kind of instability, Ding *et al.* [31] recently developed a reduced 2-DOF model in which the wheel is represented by a single mode and the track vibration behavior in the vertical direction is simplified as a mass, a spring, or a damper equivalent to the behavior of an infinite track. Instabilities of the system were observed even with a very small friction coefficient. However, the instability mechanisms still differ according to the track model. Mode coupling was found when the track is simplified as a mass. On the other hand, it seems that there is no mode coupling when the track is simplified as a damper. Ding *et al.* [31] did not compare the results obtained by the reduced model with those from the full model, thus the exact instability mechanism in this case is still unknown. This kind of instabilities should therefore be studied more closely.

The aim of this paper is to clarify the mechanisms responsible for curve squeal. By using a point-contact model and wheel/rail modal bases, a stability analysis is performed around the equilibrium state. The normal contact problem is assumed to be Hertzian. A constant Coulomb's friction law is used in the tangential problem. Full sliding equilibrium states are assumed. Section 2 presents a stability analysis of wheel/rail contact in curve by using modal bases. These bases are calculated using the stiffness and mass matrices computed from wheel and rail finite element models. Instabilities are analyzed and distinguished through the use of bifurcation curves. In order to examine in detail one kind of instability, Section 3 proposes a reduced 1-DOF model which is based on the results provided by Section 2. The contact model is similar but the wheel dynamics is represented by only one free-interface normal mode. The rail dynamics is simplified as a complex stiffness. The results obtained by this reduced model are compared with the results of the full model.

2. Stability analysis for a wheel/rail contact system in curve

2.1. Statement of the problem

The wheel/rail interaction model is described in Fig. 1.

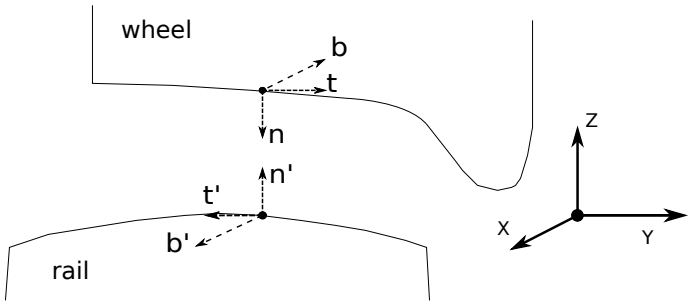

Figure 1: Reference frame of the wheel/rail interaction. The rolling direction along the rail is the $x-$ direction. The lateral direction is the $y-$ direction. The vertical direction is the $z-$direction. (n, t, b) and (n', t', b') are respectively the local frames of the wheel and the rail such that: $n' = -n = Z$, $t' = -t = -Y$, $b' = -b = X$

A loaded wheel with constant rolling speed V and angle of attack α is considered (Fig. 2). While the angle of attack α is enough small, the resulting sliding velocity is $\Delta V_y \approx V\alpha$. In the case of enforced lateral creepage $s_{yo} = \frac{\Delta V_y}{V}$, the mean dynamic lateral creepage s_y at the contact point is defined by:

$$s_y = \frac{v_y^w - v_y^r}{V} = s_{yo} + \frac{(\dot{u}_y^w - \dot{u}_y^r)}{V} \tag{1}$$

where v_y and u_y are the lateral dynamic velocity and displacement respectively. w and r denote the wheel and the rail respectively. $\dot{\bullet}$ represents the time derivative.

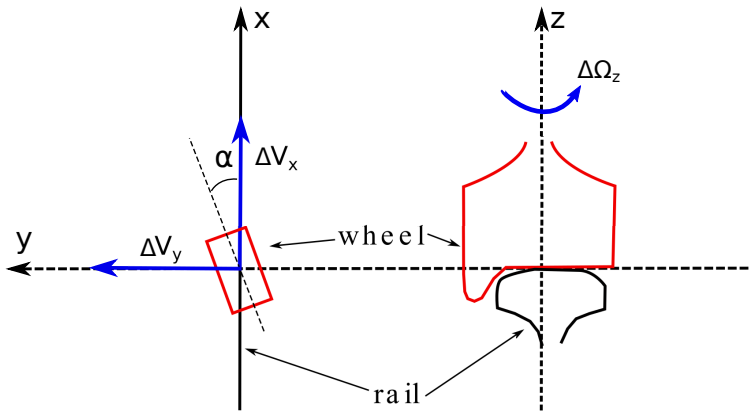

Figure 2: Coordinate system, kinetic variables (α: angle of attack of the curve, ΔV_y: imposed lateral sliding velocity, ΔV_x: imposed longitudinal sliding velocity and $\Delta\Omega_z$: imposed spin velocity)

Two major assumptions are made. Firstly, the normal contact is Hertzian so that the normal contact force can be analytically determined. Secondly, the lateral friction force satisfies the Coulomb law in the full sliding phase with a constant friction coefficient μ.

2.2. Wheel and rail dynamics

It is assumed that the wheel and the rail are represented by normal modal bases $\mathbf{\Phi}$. These wheel and rail normal modal bases are made of the eigenvectors of the eigenvalue problem:

$$\mathbf{K\Phi} = \omega^2 \mathbf{M\Phi} \tag{2}$$

where ω is the natural pulsation. $\mathbf{K}$ and $\mathbf{M}$ are the stiffness and mass matrices respectively. These matrices $\mathbf{K}$ and $\mathbf{M}$ are provided by wheel/rail FE models which are presented in section 2.5. These bases $\mathbf{\Phi}$ are then normalized with respect to mass so that $\mathbf{\Phi}^{\mathrm{T}}\mathbf{M\Phi} = \mathbf{I}$. Theses bases are calculated using classical solvers IRA/Sorensen of the ARPACK or the Lanczos library, both available in Matlab's SDT Toolbox.

At the contact point, the vertical and lateral displacements of wheel and rail can be written as:

$$\begin{aligned} u_z^{(w,r)} &= \mathbf{\Phi_z}^{(w,r)}\mathbf{q} \\ u_y^{(w,r)} &= \mathbf{\Phi_y}^{(w,r)}\mathbf{q} \end{aligned} \tag{3}$$

where (w, r) denote wheel and rail. $\mathbf{\Phi_z}^{(w,r)}$ and $\mathbf{\Phi_y}^{(w,r)}$ are the vectors of vertical and lateral modal amplitudes at the contact point on the wheel and the rail. $\mathbf{q}$ denotes the unknown generalized coordinates vector. The size of vector $\mathbf{q}$ is m where m is the total number of modes in the normal modal bases.

2.3. Contact mechanics

In the normal direction n, a linearized Hertz's stiffness ([33]) can be applied for small amplitudes of displacement:

$$k^H = \frac{3}{2}\frac{F_n}{\delta} \tag{4}$$

where F_n is the static normal contact force and δ is the static penetration caused by the load F_n at the contact point. The dynamic perturbation f_n of the normal force can be expressed through the contact stiffness as:

$$f_n = -k^H u_n \tag{5}$$

where $u_n = u_z^r - u_z^w = (-\mathbf{\Phi_z^w} + \mathbf{\Phi_z^r})\mathbf{q}$ is the dynamic relative displacement between the wheel and the rail in the normal direction n.

In tangential direction t, a Coulomb's friction law is assumed and a full sliding contact state is considered. The relation between the dynamic perturbation f_t of the tangential contact force and the dynamic perturbation of the normal contact force f_n is then given by:

$$f_t = \mu f_n \mathrm{sign}(s_y) \tag{6}$$

where sign(•) denotes the sign of (•). In the full sliding state, $\mathrm{sign}(s_y) = \mathrm{sign}(s_{yo})$.

2.4. Stability analysis

By using the normal modal bases, the linearized equation of motion around the total sliding equilibrium in the global frame is written as:

$$\mathbf{M_{red}}\ddot{\mathbf{q}} + \mathbf{C_{red}}\dot{\mathbf{q}} + \mathbf{K_{red}}\mathbf{q} = (-\mathbf{\Phi_z^w} + \mathbf{\Phi_z^r})^{\mathrm{T}} f_n + (\mathbf{\Phi_y^w} - \mathbf{\Phi_y^r})^{\mathrm{T}} f_t \tag{7}$$

where $\mathbf{q}$ is the dynamic perturbation of generalized coordinates vector around the total sliding equilibrium. $\mathbf{M_{red}}$, $\mathbf{K_{red}}$, $\mathbf{C_{red}}$ are the reduced mass, stiffness and viscous damping matrix of the whole system and come from the combination of wheel and track reduced matrices detailed in the following sections. Matrix $\mathbf{K_{red}}$ is generally a diagonal matrix containing the squared natural pulsations of the wheel and the rail. $\mathbf{C_{red}}$ depends on the chosen viscous damping model with extra diagonal terms in the case of non proportional damping cases. $\mathbf{M_{red}}$ is an identity matrix $\mathbf{I}$ due to the normalization of the wheel/rail modes with respect to mass.

Hence, combining with Eqs. (5) and (6), an eigenvalue problem can be obtained from Eq. (7) given by:

$$\mathbf{M_{red}}\ddot{\mathbf{q}} + \mathbf{C_{red}}\dot{\mathbf{q}} + \left(\mathbf{K_{red}} + \mathbf{K}_\mu\right)\mathbf{q} = 0 \tag{8}$$

where $\mathbf{K}_\mu = k^H \left(-\mathbf{\Phi}_z^w + \mathbf{\Phi}_z^r\right)^{\mathrm{T}} + \mu \, \mathrm{sign}(s_y)(\mathbf{\Phi}_y^w - \mathbf{\Phi}_y^r)^{\mathrm{T}}\Big)(-\mathbf{\Phi}_z^w + \mathbf{\Phi}_z^r)$. This matrix is not symmetric due to the coupling of the normal and tangential dynamics with a non-zero friction coefficient μ.

The solution of Eq. (8) is sought in the form: $\mathbf{q} = \mathbf{q_o}e^{\lambda t}$ where $\mathbf{q_o}$ is the complex amplitude of $\mathbf{q}$ and λ is a complex number. Eq. (8) becomes:

$$\left(\lambda^2\mathbf{M_{red}} + \mathbf{C_{red}}\lambda + \left(\mathbf{K_{red}} + \mathbf{K}_\mu\right)\right)\mathbf{q_o} = 0 \tag{9}$$

If the real part of λ is positive, the system becomes unstable. A perturbation of the equilibrium leads to an increasing vibration with deformations and frequencies related to the unstable modes. The divergence rate of a mode is defined as the ratio between the real and imaginary part of the complex mode:

$$DvR = \mathrm{Real}(\lambda)/\mathrm{Imag}(\lambda) \tag{10}$$

where $\mathrm{Real}(\lambda)$ and $\mathrm{Imag}(\lambda)$ are the real and imaginary parts of the associated complex mode.

2.5. Wheel and rail FE models for modal bases calculation

In this section, the finite element (FE) wheel and rail models as well as modal bases for the numerical application are presented. These models allow for an extraction of the stiffness and mass matrices which are then used to calculate normal modal bases and the reduced stiffness, mass and viscous damping matrices in the Eq. (7).

2.5.1. Wheel model

The considered wheel model is a wheel of type "Vyksa BA005" with a nominal rolling diameter of 920 mm and a mass of 314 kg (Fig. 3). The material data of the wheel are listed in Tab. 1. A rigid constraint is applied at the inner face of the hub, where the wheel is connected to the axle. This boundary condition avoids rigid mode in the modal basis.

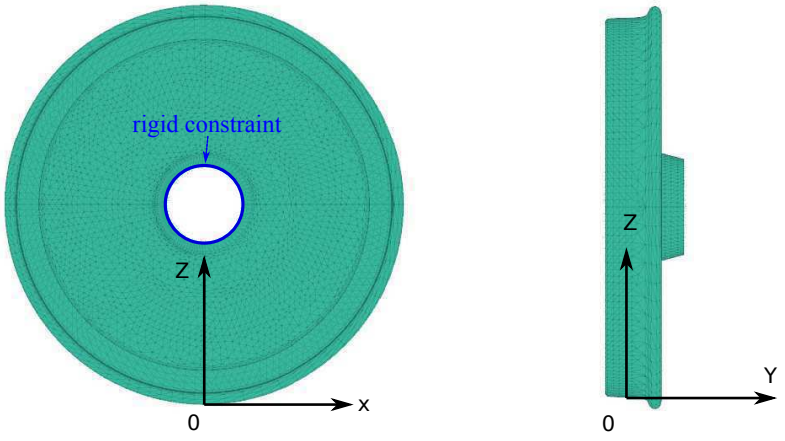

(a) XOZ plan **(b)** YOZ plan

Figure 3: Wheel FEM mesh (wheel of type "Vyksa BA005" with a nominal rolling diameter of 920 mm and a mass of 314 kg) with a rigid constraint applied at the inner face of the hub, where the wheel is connected to the axle.

In this paper, only high lateral slip of the wheel on the rail-head is considered as the main cause of curve squeal, the corresponding frequency range is up to 5000 Hz [2]. The 60 first natural frequencies and corresponding free-interface modes have then been calculated up to 5000 Hz using Eq. (2). As in [29, 30, 34], three types of mode may

Data	Wheel	Rail
Young's modulus (GPa)	206.9	205
Poisson's ratio	0.288	0.3
Density (kg/m^3)	7800	7800

Table 1: Material data of the wheel and the rail

be distinguished: the radial modes (r, n_d), the axial modes (a, n_c, n_d) and the circumferential modes (c, n_c, n_d), where n_d is the number of nodal diameters and n_c is the number of nodal circles. In order to validate the wheel FE model, the mesh has been refined until the normal frequencies converge in the frequency range of interest. Fig. 4 presents the relative frequency difference as a function of mesh size for the main wheel modes which are considered prone to squeal in the literature [3, 6]. The chosen FE mesh (see Fig. 3) is made of 70300 tetra quadratic elements with mesh size length of 15mm. The choice of the mesh size length of 15mm ensures a relatively good quality (the relative frequency difference is inferior to 0.15%). On the other hand, the corresponding number of DOFs of the model is not too large to stock the wheel nomal basis (500000 DOFs) and to work more easily with a computer of 8GB RAM.

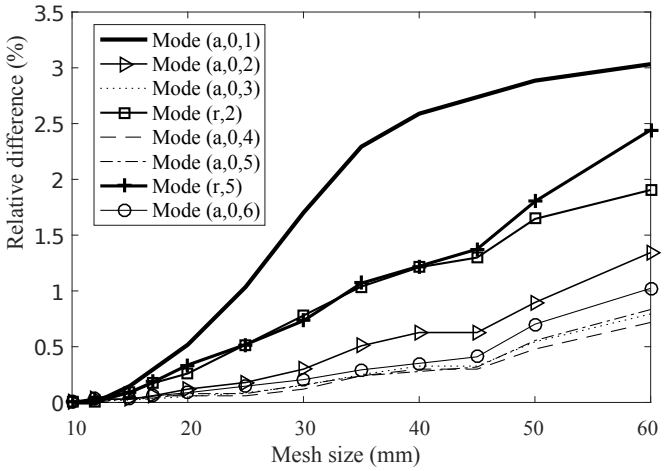

Figure 4: Relative difference of some wheel normal frequencies as a function of mesh size (Reference mesh size:1cm)

The corresponding modes types and frequencies are listed in Tab. 2 where "double" means that there are two wheel modes of the same type with same frequency due to the symmetry of the wheel. Some typical mode shapes are shown in Fig. 5.

Classical modal damping factors ξ^w are chosen depending on the nodal diameters [33]:

$$\begin{cases} \xi^w = 10^{-3} & \text{if} \quad n_d = 0 \\ \xi^w = 10^{-2} & \text{if} \quad n_d = 1 \\ \xi^w = 10^{-4} & \text{if} \quad n_d \geq 2 \end{cases} \tag{11}$$

The reduced stiffness matrix $\mathbf{K^w_{red}}$ corresponding to this wheel normal basis is generally a diagonal matrix containing the squared natural pulsations ω_i:

$$\mathbf{K^w_{red}} = \begin{bmatrix} \omega_1^2 & & \\ & \ddots & \\ & & \omega_{60}^2 \end{bmatrix} \tag{12}$$

while the reduced viscous damping matrix $\mathbf{C^w_{red}}$ is a diagonal matrix containing the damping factors ξ_i^w multiplied by

Mode number	Type		Frequencies (Hz)	Mode number	Type		Frequencies (Hz)
1,2	a,0,1	double	135	31	a,1,0		3238
3	a,0,0		226	32,33	r,5	double	3280
4,5	a,0,2	double	335	34,35	a,1,1	double	3356
6	c,0		445	36,37	a,0,6	double	3419
7,8	r,0	double	659	38,39	a,1,4	double	3541
9,10	a,0,3	double	920	40,41	a,1,2	double	3614
11,12	r,2	double	1155	42,43	r,6	double	4074
13,14	a,1,0	double	1494	44,45	a,1,3	double	4310
15,16	a,0,4	double	1671	46,47	c,2	double	4313
17,18	a,1,1	double	1709	48,49	a,0,7	double	4350
19,20	r,3	double	1833	50,51	a,1,5	double	4390
21	r,0		2059	52	a,2,0		4704
22,23	a,1,2	double	2152	53	a,2,1		4733
24	a,0,5		2519	54	a,3,0		4747
25,26	r,4	double	2543	55,56	a,2,2	double	4854
27,28	r,1	double	2683	57,58	r,7	double	4931
29,30	a,1,3	double	2774	59,60	a,2,4	double	5054

Table 2: Wheel FE modal basis

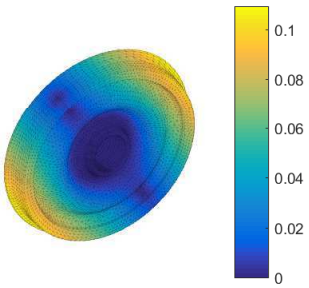

(a) Mode axial of 135 Hz

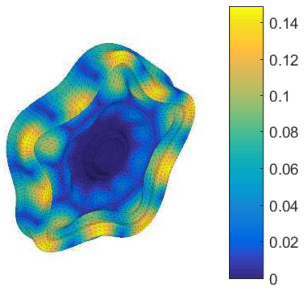

(b) Mode radial of 3280 Hz

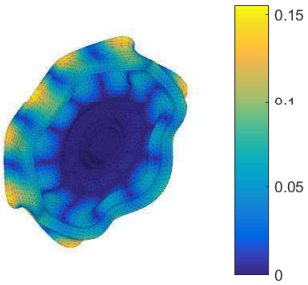

(c) Mode axial of 3419 Hz

Figure 5: Wheel natural free-interface mode shape

the natural pulsations of wheel:

$$\mathbf{C^w_{red}} = \begin{bmatrix} 2\xi_1^w\omega_1 & & \\ & \ddots & \\ & & 2\xi_{60}^w\omega_{60} \end{bmatrix} \tag{13}$$

2.5.2. Track model

Unlike the wheel, the rail is an infinite structure in the longitudinal direction which induces some advantages but also some drawbacks for the modeling. The main advantage is that the rail can be modeled using beam-like structures in a wide frequency range, for which analytical or semi-analytical solutions exist. Cross-sectional deformation has to be taken into account only at high frequency for which numerical methods with rail section discretization has to be used. The drawback is that the vibratory behavior is not modal but the result of propagating waves in the longitudinal direction. This is not a problem in the case of equations formulated in the frequency domain with point mobilities, however, this can be unfavorable to other methods like time-domain modeling or model reduction.

Considering that the effects of the rail could be neglected due to the high flexibility of the wheel at squeal frequencies, the rail dynamics was not included in the models proposed by Rudd [5], Van Ruiten [35], Schneider *et al.* [18], Heckl *et al.* [21, 22], Chiello *et al.* [23], Brunel *et al.* [26] or Glocker *et al.* [6].

The rail vertical and lateral dynamics was included through point mobilities obtained from the TWINS software [36] in Debeer *et al.* [25], Xie *et al.* [37], Hsu *et al.* [38] and Squicciarini [39]'s models. There are three available modules in TWINS for the track dynamics. In case of ballasted tracks, the first two modules use analytical models of a Timoshenko beam in vertical and lateral bending, mounted on a two-layer continuous (Rodel) or periodic support. Pads and ballast are modeled by springs whereas sleepers are considered as rigid masses. The damping of the pads and ballast is taken into account by structural loss factors rather than viscous dampers. The third module includes the deformation of the rail cross-section. This is particularly important at high frequencies (above 1 or 3 kHz according to the vertical or lateral bending). A short length of rail, modeled with finite elements, is joined end to end to form an infinite model using periodic structure or transfer matrix theory. As well as the rail, the pad, sleeper and ballast are also included using finite element matrices [40]. However, since the support is continuous, this last model can not predict the behavior associated with the "pinned-pinned" effect. Indeed, depending on the location of the excitation, resonances or anti-resonances occur at frequencies when the half of the wavelengths of the propagating waves in the rail are close to the length of the sleeper span. In Pieringer [28] and Zenzerovic *et al.* [29, 30]'s models, the lateral, vertical and longitudinal rail dynamics are modeled using waveguide finite elements (WFE) [41]. Considering that the rail has a constant cross-section in the longitudinal direction, a wave-type solution is assumed along the rail. The model takes into account the cross-sectional deformations of the rail. However, in this model, the support is continuous. It can not predict the behavior associated with the "pinned- pinned" effect.

In this section, a FE track model which can overcome the limits of these models above is used. In order to avoid the reflexion of waves in a FE model, anechoic terminations are modeled by gradually increasing the rail damping at its termination, as proposed for instance in [42]. The track model consists in one periodically supported rail of UIC60 type (Fig. 6). This rail is 48 m long. The space between the sleepers (sleeper span) is 60 cm. The FE track model is made of 200000 quadratic elements and 600000 DOFs. As a first approach, the dynamics of the sleepers and the ballast is neglected because of its rather low frequency domain. The track support contains only elastic pads that connect the rail and each sleeper. They are modeled by 69 springs of longitudinal, lateral and vertical stiffnesses ($Kx = Ky = 36, Kz = 180$) MN/m for each sleeper. The pad structural damping is set to $\eta_s = 1$. The contact position is in the center of the rail in the $x-$axis. The rail structural damping is $\eta = 0.02$. The terminations are obtained by gradually increasing the rail damping from 2% to 100 % [42].

Finally, a complex stiffness matrix $\hat{\mathbf{K}}^{\mathbf{r}}$ is obtained which includes the real stiffness matrix $\mathbf{K^r}$ and the damping matrix $\mathbf{K^r_{imag}}$, given by $\hat{\mathbf{K}}^{\mathbf{r}} = \mathbf{K^r} + j\mathbf{K^r_{imag}}$ where $\mathbf{K^r_{imag}}$ is piecewise proportional to $\mathbf{K^r}$ according to the different structural damping factors. At this point, no viscous damping is introduced for the track ($\mathbf{C^r} = \mathbf{0}$).

The 1700 natural frequencies and corresponding free-interface modes Φ^r have been calculated up to 5000 Hz using only the real stiffness matrix $\mathbf{K^r}$ from the Eq. (2). The proposed track model is validated by calculating its dynamic mobilities and comparing these mobilities with the results obtained by analytical models (Timoshenko beam models).

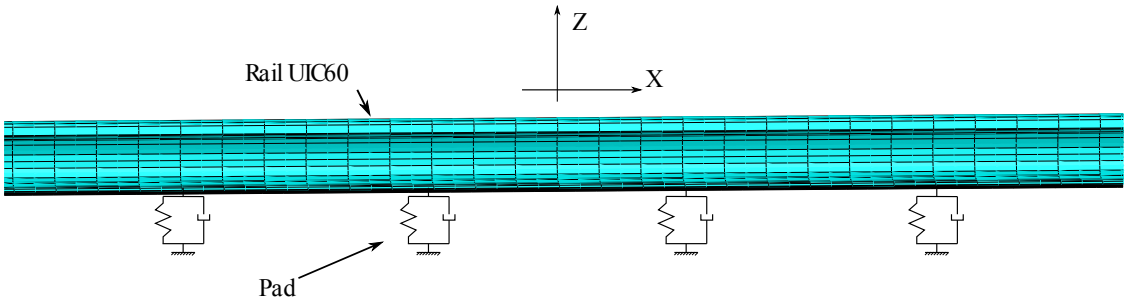

Figure 6: Track model (Rail of type UIC60 with periodical supports (pad))

The dynamic mobilities at the contact point are computed by using the reduced basis including the free-interface modes $\mathbf{\Phi^r}$. For each frequency ω, the mobility at contact DOF i_1 due to a force at contact DOF i_2 is given by:

$$V_c^{i_1,i_2}(\omega) = j\omega \mathbf{\Phi^r}(i_1,:)\left(-\omega^2 \mathbf{M_{red}}^r + \hat{\mathbf{K}}^r_{\mathbf{red}}\right)^{-1} \mathbf{\Phi^r}(i_2,:)^{\mathrm{T}} \tag{14}$$

where $\hat{\mathbf{K}}^r_{\mathbf{red}} = \mathbf{\Phi^r}^{\mathrm{T}} \hat{\mathbf{K}}^{\mathbf{r}} \mathbf{\Phi^r}$ and $\hat{\mathbf{M}}^r_{\mathbf{red}} = \mathbf{\Phi^r}^{\mathrm{T}} \mathbf{M^r} \mathbf{\Phi^r} = \mathbf{I}$ are the (non diagonal) reduced complex stiffness and the reduced mass matrix respectively.

The amplitude and phase of the track vertical and lateral point mobilities at the center point between two sleepers are represented in Figs. 7 and 8. Two resonant frequencies $f = 1059$ Hz and $f = 503$ Hz are observed on the mobility curves respectively for the cases of lateral and vertical loads. These frequencies correspond to the pinned-pinned frequencies.

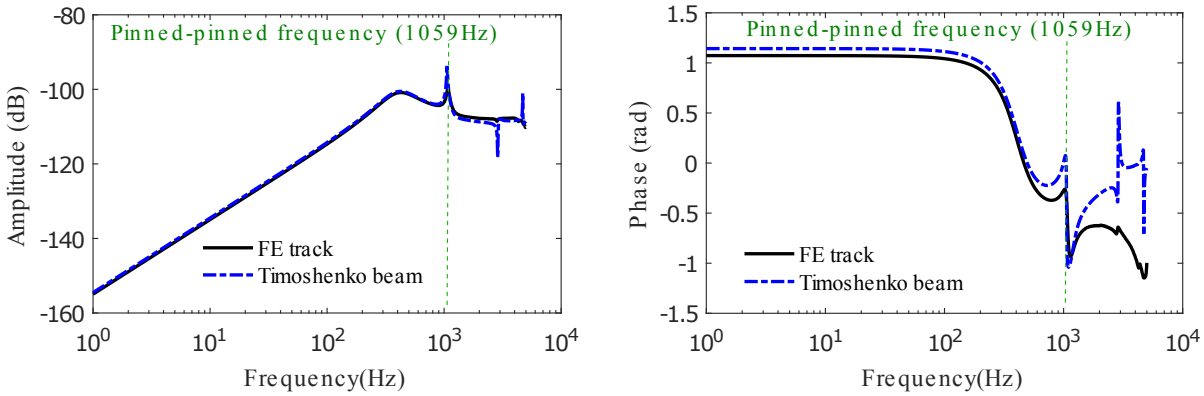

(a) Amplitude **(b)** Phase

Figure 7: Vertical mobility at contact point (Reference amplitude: 1 m/s/N)

The dynamic response obtained by FEM is compared with the analytical Timoshenko beam [43] in vertical bending in Fig. 7. The frequencies of the peaks of the FE track are close to those from Timoshenko beam model. However between the FE track and Timoshenko beam model, there are some differences in the amplitudes at the resonance peak that are related to the distance between two sleepers. This difference results from the spreading of the springs that connect the rail and the sleepers in the FE model. In the Timoshenko beam, there is only one spring that connects the rail and the sleepers. The evolution of the curves for high frequencies (> 3000 Hz) is also different. This is due to the cross-sectional deformations which are not taken into account in the Timoshenko beam. For the lateral vibration, no comparison is proposed since a pertinent analytical model should include both bending and torsional deformations and is only valid at low frequencies.

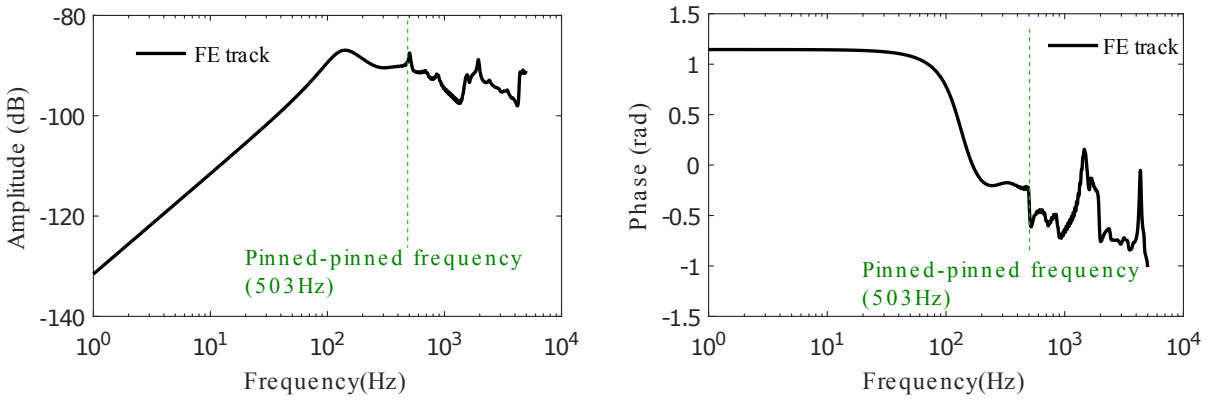

(a) Amplitude **(b)** Phase

Figure 8: Lateral mobility at contact point (Reference amplitude: 1 m/s/N)

Concerning the rail anechoic termination, the amplitude of the vertical response along the track caused by the impulsion at the contact point ($x = 0$) at some frequencies is presented in Fig. 9. The amplitude of this mobility decreases along the track and there is no wave reflection.

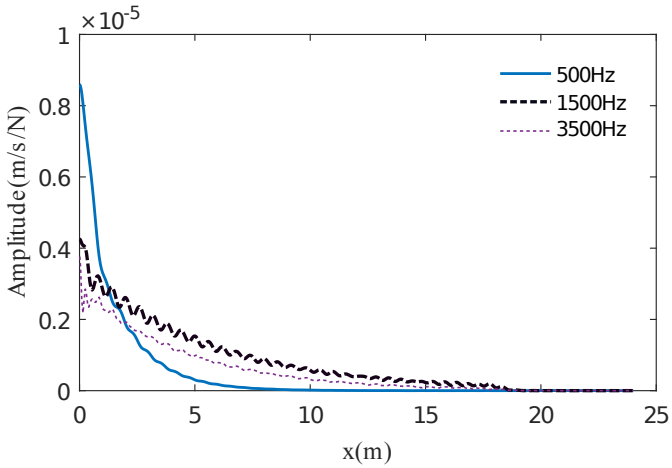

Figure 9: Vertical mobility along the track caused by the impulsion at the contact point ($x = 0$)

Finally, the reduced mass, stiffness and viscous damping matrix of the whole system $\mathbf{M_{red}}$, $\mathbf{K_{red}}$, $\mathbf{C_{red}}$ used in Eq. (9) are given by:

$$\begin{aligned} \mathbf{M_{red}} &= \mathbf{I} \\ \mathbf{C_{red}} &= \begin{bmatrix} \mathbf{C^w_{red}} & \\ & \mathbf{0} \end{bmatrix} \\ \mathbf{K_{red}} &= \begin{bmatrix} \mathbf{K^w_{red}} & \\ & \hat{\mathbf{K}}^{\mathbf{r}} \end{bmatrix} \end{aligned} \tag{15}$$

2.6. Numerical results

In this section, in order to study the effect of the track dynamics, a case with rigid track and another case with flexible track are studied. In each case, the results of stability analysis of the wheel/rail system obtained from Eq. (9) using the reference data listed in Table 3 are firstly presented. To analyze the instability mechanism, it is useful to compute the bifurcation curves representing the evolution of the unstable modes as a function of friction coefficient μ while the other parameters are kept constant.

Rolling velocity V (m/s)	10
Imposed lateral velocity of the wheel V_y (m/s)	0.1
Friction coefficient μ	0.3
Static vertical load N	7 kN

Table 3: Kinematic parameters of the wheel/rail rolling contact model

2.6.1. Rigid track

The rigid track case is obtained by neglecting all contributions of the track in the system. In this case, there is no unstable mode (with positive real part) using the reference data in Table 3.

The bifurcation curves are represented in Fig. 10. One unstable mode appears when friction coefficient μ reaches a critical value at which the complex modes frequencies coalesce. This critical μ is about 0.94 without any wheel damping and $\mu = 0.58$ with wheel damping. The corresponding unstable frequency is 3391 Hz and with the mode shape presented in Fig. 11.

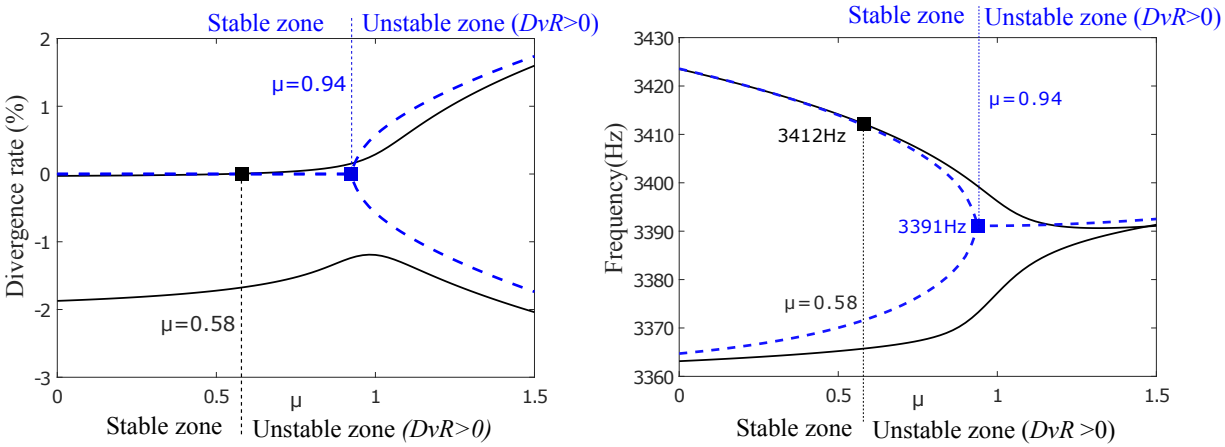

(a) Divergence rate **(b)** Frequency

Figure 10: Bifurcation curves in the case with rigid track (black line: with wheel damping, blue line: without wheel damping)

Even if the frequency of this unstable mode gets close to the axial wheel mode with 6 nodal diameters and 0 nodal circle (3419Hz), the mode shape is significantly different. In order to find the contributions of the free wheel modes in this unstable complex mode, the *Normalized Modal Assurance Criterion* (MAC) [44] between wheel normal modes and this unstable complex mode is calculated. The expression of the MAC used here is given by Eq. (16) in which $\mathbf{\Phi}_{complex}$ is the unstable complex mode and $\mathbf{\Phi}_i^w$ is a free normal wheel mode.

$$\mathbf{MAC}(\mathbf{\Phi}_i^w, \mathbf{\Phi}_{complex}) = \frac{|(\mathbf{\Phi}_i^w)^{\mathrm{T}} \mathbf{M}^w \mathbf{\Phi}_{complex}|^2}{|\mathbf{\Phi}_i^{w\mathrm{T}} \mathbf{M}^w \mathbf{\Phi}_i^w||\mathbf{\Phi}_{complex}^{\mathrm{T}} \mathbf{M}^w \mathbf{\Phi}_{complex}|} \tag{16}$$

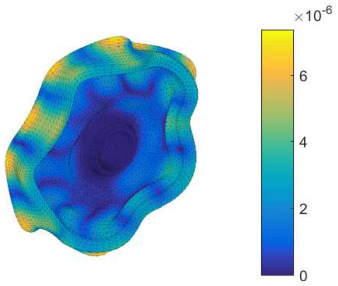

Figure 11: Unstable mode shape with the rigid track

With this criterion, five natural wheel modes are found to be involved in the unstable complex mode: the radial mode (r,5) of frequency 3280 Hz, the "double" axial modes (a,1,1) of frequency 3356 Hz and the "double" axial modes (a,0,6) of frequency 3420 Hz. The contribution of the axial modes (a,0,6) is the greatest.

Concerning the instability mechanism, it is firstly found that the form of the bifurcation curve is similar to classical mode coupling curves, given for instance by Hoffman [14]. Therefore, the instability mechanism is mode coupling. Moreover, there is a strong contribution of several wheel modes in the unstable mode.

2.6.2. Flexible track

With the flexible track, the results change radically. Fig. 12 shows four unstable modes (with positive real part) obtained using the reference data in Table 3. The frequency of these unstable complex modes are 334, 918.3, 1671 and 3418 Hz respectively which get close to the frequencies of the 4 axial wheel modes with (2,3,4,6) nodal diameters and 0 nodal circle (Figure 13).

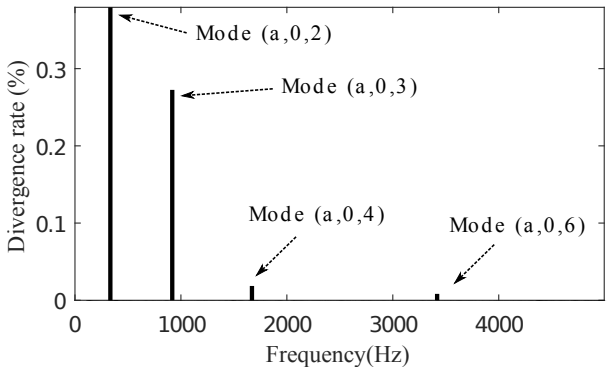

Figure 12: Divergence rate of the complex modes with the flexible track

The first three modes shapes are close to the 3 axial wheel modes with (2,3,4) nodal diameters and 0 nodal circle respectively (Fig. 13a, Fig. 13b and Fig. 13c). This result is coherent with the experimental observation that the squeal fundamental frequencies correspond to axial wheel modes with zero nodal circles, in agreement with the literature review [3, 4]. Like in the case with a rigid track, five natural wheel modes are involved in the fourth complex mode (Figure 13d).

Bifurcations curves

The bifurcation curves of the unstable complex modes in the case with flexible track are presented in Fig. 14. The critical friction from which the complex modes become unstable are respectively 0.06, 0.1, 0.22 and 0.3 for the unstable complex modes (a,0,2), (a,0,3), (a,0,4) and (a,0,6).

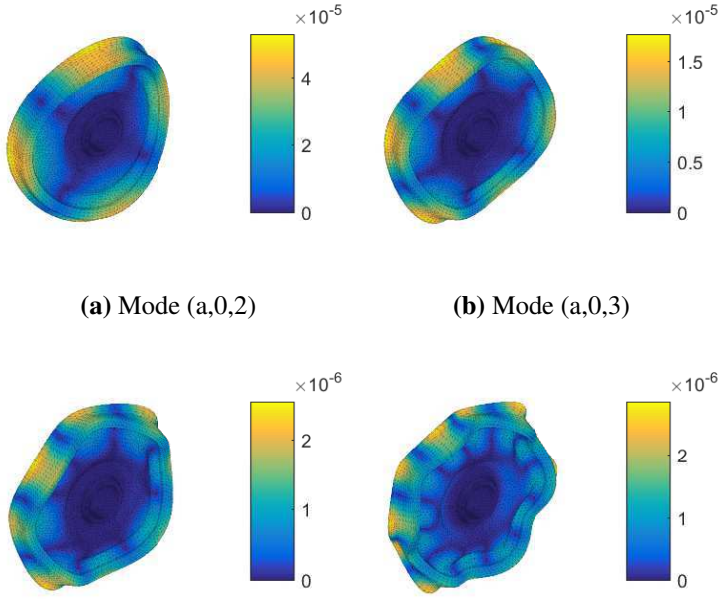

(a) Mode (a,0,2) **(b)** Mode (a,0,3)

(c) Mode (a,0,4) **(d)** Mode (a,0,6)

Figure 13: Unstable modes shapes with the flexible track

For the first three unstable modes (a,0,2), (a,0,3) and (a,0,4), the form of the bifurcation curves that seems to be linear is not the same as the form of the bifurcation curves in case of mode coupling [14]. Moreover, the zoom near the unstable frequency (a,0,3) in Fig. 15 does not show coalescence of any frequencies. Results are similar for the unstable modes (a,0,2) and (a,0,4). Actually, one can imagine that these instabilities are not due to mode coupling. According to Ding *et al.* [24], this instability is due to coupling between the normal and tangential components of the single wheel mode when the rail dynamics is included.

On the other hand, the bifurcation curves in Fig. 14d shows a coupling between two complex modes. However, there is no perfect coalescence between the two frequencies due to the system damping.

Effect of the rail lateral dynamics

In the case with the rail dynamics, one can determine separately the role of the rail vertical and lateral dynamics. In Eq. (8), the rail lateral dynamics can be neglected by eliminating the term $\mathbf{\Phi}_y^r$. With the data from the reference case, Fig. 16 shows that the instability does not depend on the lateral flexibility of the rail. The rail vertical dynamics is therefore the most important characteristic for the occurrence of instability. Ding *et al.* [24, 31] stated that the rail dynamics can change the flexibility of the normal contact, which affects the level of coupling. With our results, one can also conclude more specifically that only the rail vertical dynamics changes the flexibility of the normal contact.

In this section, it is found that instabilities change radically with the flexible track compared to the rigid track. The unstable modes with (2,3,4,6) nodal diameter and 0 nodal circle are found in the case of flexible track, which is consistent with experimental observations [3, 4, 17]. Concerning the instability mechanisms, with the rigid track, mode coupling is responsible for instabilities. With the flexible track, mode coupling and coupling between the normal and tangential components of a single wheel mode combining with the track vertical dynamic can coexist.

In order to explain the second type of instabilities, Ding *et al.* [31] recently developed a 2-DOF model in which the wheel is represented by a single mode and the track vibration behavior in the vertical direction is simplified as a mass, a spring, or a damper. For the damper case, there is no mode-coupling and the evolution of the bifurcation curve is linear. On the other hand, for the mass case, mode coupling is considered responsible for these instabilities. A question stands out concerning the exact equivalent behavior of an infinite rail (mass or damper) responsible for

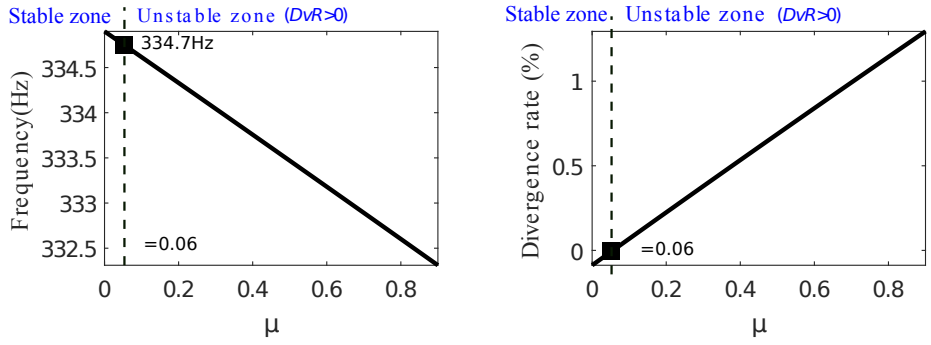

(a) Mode (a,0,2)

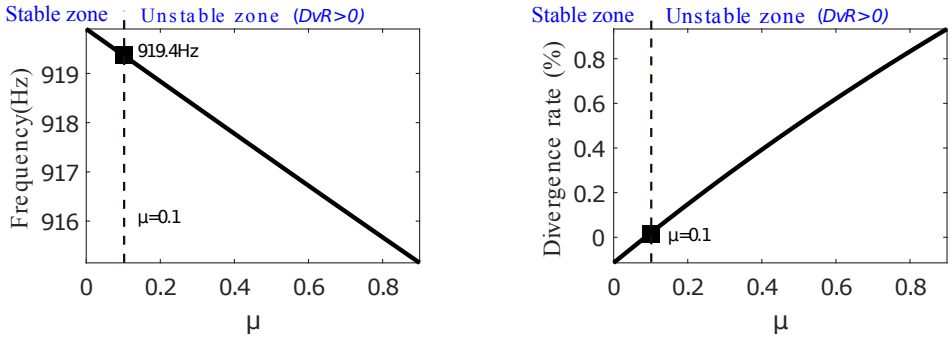

(b) Mode (a,0,3)

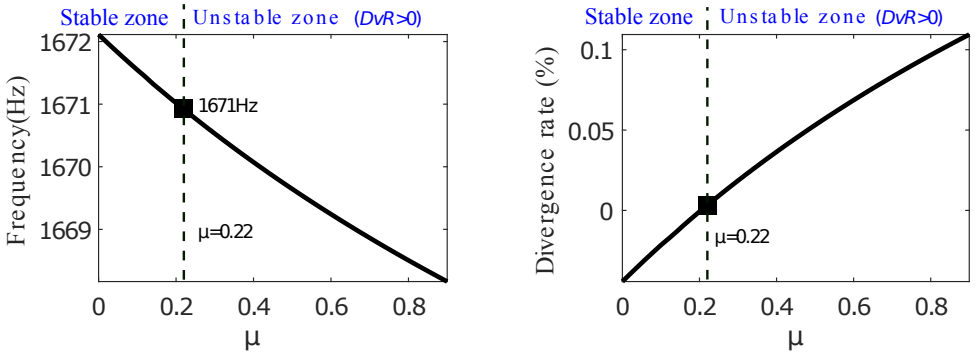

(c) Mode (a,0,4)

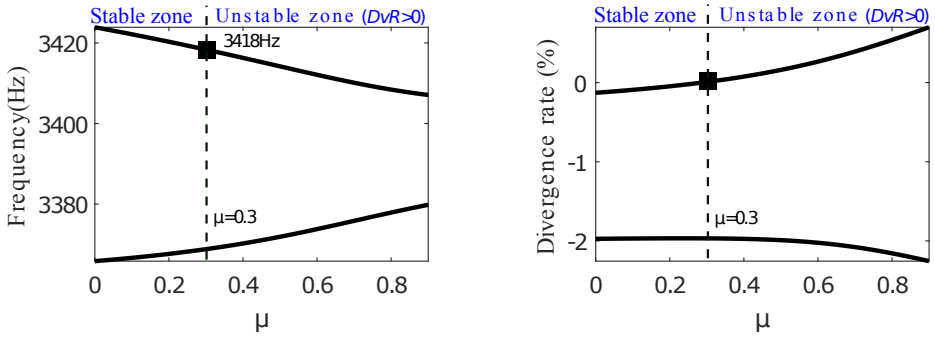

(d) Mode (a,0,6)

Figure 14: Bifurcation curves of the unstable complex modes with the flexible track (■: a critical point from which instabilities appear)

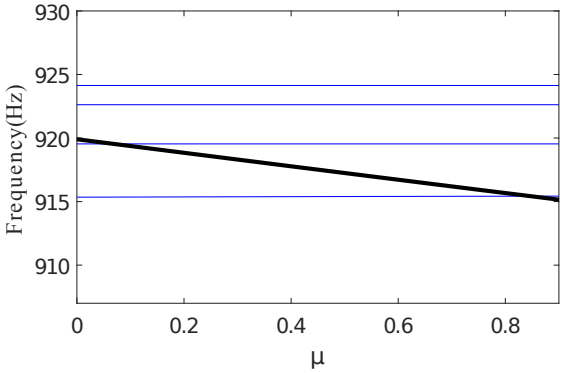

Figure 15: Zoom near the unstable mode (a,0,2) frequency (black)

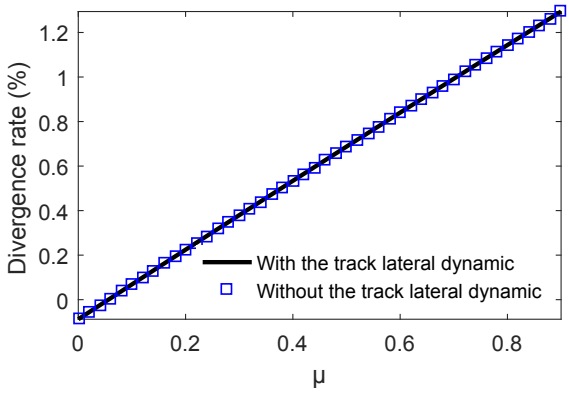

(a) Mode (a,0,2)

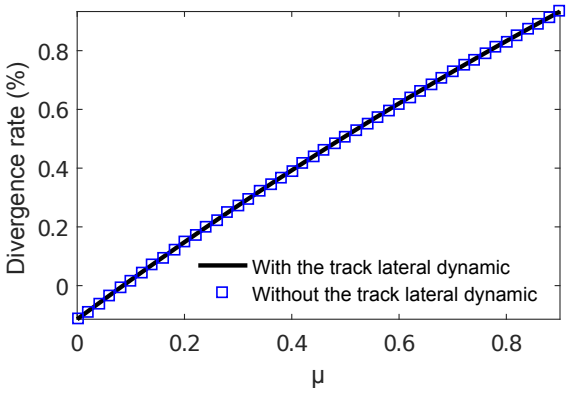

(b) Mode (a,0,3)

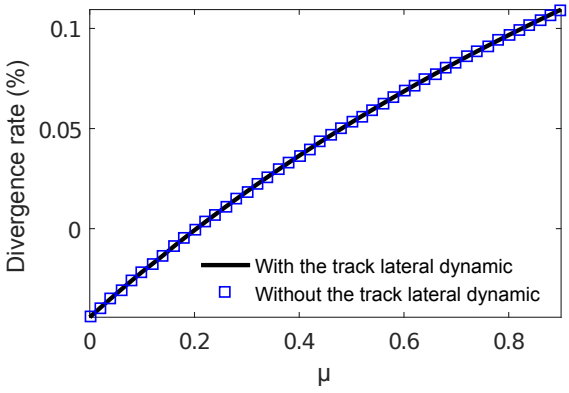

(c) Mode (a,0,4)

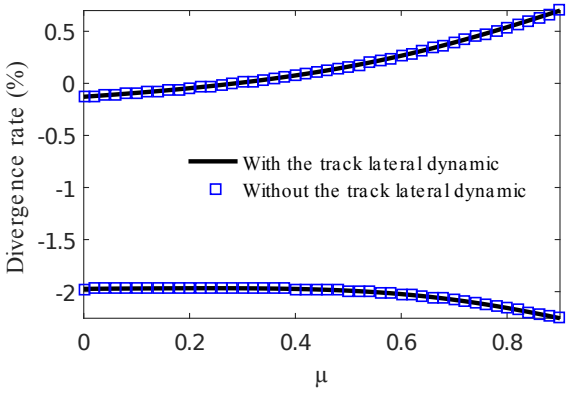

(d) Mode (a,0,6)

Figure 16: Bifurcation curves of unstable complex modes with and without the lateral flexibility of the rail

these instabilities. This is the main reason that in the following section, a reduced model allowing to explain the kind of instabilities is developed. The results obtained by this reduced model are then compared with those obtained by the full model.

3. Clarification of the effect of rail vertical phase response in railway curve squeal generation

3.1. Description of the model

In the previous section, it is found that the coupling between a single wheel mode and the rail vertical dynamics can lead to instability. This instability occurs without falling friction nor mode coupling, which are the two mechanisms considered in most models to simulate friction-induced vibrations. Considering a single wheel mode combined with the track vertical dynamics seems to be sufficient to obtain this type of instability. This is studied through a simplified model as shown in Fig. 17.

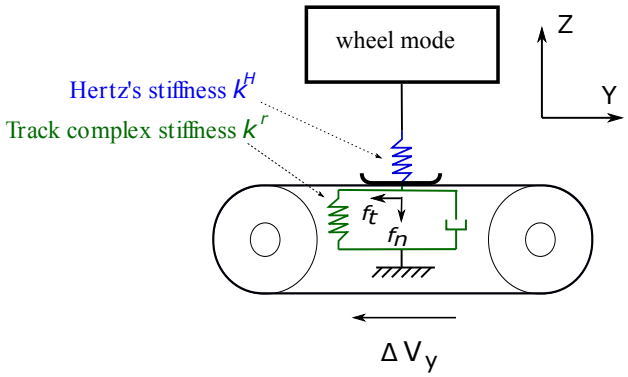

Figure 17: Simple 1-DOF model for instabilities due to the rail vertical phase response

The mechanical system is represented by one wheel mode of natural pulsation Ω, damping factor ξ^w and contact modal amplitudes Φ_z^w and Φ_y^w, coupling with an Hertz'stiffness k^H representing the contact [33] and an equivalent complex stiffness k^r representing the track vertical dynamics. This track complex stiffness k^r is obtained by:

$$k^r(\omega) = \frac{i\omega}{V_c(\omega)} \tag{17}$$

where $V_c(\omega)$ is the vertical mobility due to a vertical force at the contact point (Eq. (14)).

It is worth to note that the imaginary part of complex stiffness k^r is non-zero and represents a phase shift in the contact point mobilities of the rail. This imaginary part may be considered as a damper equivalent to the behavior of an infinite track. This damper is mainly due to the phase shift of the propagating wave but also to structural damping effects [33].

The equivalent stiffness k^v is defined as the series springs combining the Hertz's stiffness k^H and the track vertical complex stiffness k^r:

$$k^v = \frac{k^H k^r}{k^H + k^r} \tag{18}$$

The dynamic vertical and lateral contact forces f_n and f_t are calculated from the full sliding condition:

$$f_n = -k^v u_n^w \tag{19a}$$

$$f_t = \mu f_n \, \mathrm{sign}(s_y) \tag{19b}$$

where $u_n^w = -\Phi_z^w q$ is the vertical displacement at the contact point in the local frame of the wheel. q denotes the unknown generalized coordinate corresponding to the wheel mode. $s_y = s_{y0}$ is the lateral creepage of the wheel.

Under the above assumptions, the linearized equations of the system is written:

$$\ddot{q} + 2\xi^w \Omega \dot{q} + \Omega^2 q = -\Phi_z^w f_n + \Phi_y^w f_t \tag{20}$$

This equation is written in the modal basis as in section section 2. However, this modal basis includes only a wheel mode.

3.2. Stability analysis

By assuming a harmonic dependence for all dynamic variables X such that $X = X_o(\omega)e^{i\omega t}$, Eq. (20) becomes:

$$(-\omega^2 + 2i\omega\xi^w\Omega + \Omega^2)q = -\Phi_z^w f_n + \Phi_y^w f_t \tag{21}$$

Combining with Eq. (19), Eq. (21) leads to an eigenvalue equation:

$$\left(-\omega^2 + 2i\omega\xi^w\Omega + \Omega^2 + K_c\right) q = 0 \tag{22}$$

where

$$K_c = \left(\Phi_z^w - \mu \text{sign}(s_{y0})\Phi_y^w\right) k^v \Phi_z^w \tag{23}$$

is the complex stiffness due to the contact, the friction, the wheel modal amplitudes and the rail vertical dynamics. The imaginary part of this complex stiffness K_c results from the imaginary part of the rail stiffness. In other words, it results from the damping and the propagative waves of the rail. An equivalent viscous damping can be introduced:

$$c_c(\omega) = \frac{\text{Imag}(K_c)}{\omega} \tag{24}$$

where Imag(•) denotes respectively the imaginary part of (•) .

This damping can be expressed by a modal damping factor:

$$\eta_c(\omega) = \frac{c_c}{2\Omega} \tag{25}$$

Fig. 18 shows the vertical mobility of the wheel and the track on the contact point ($x = 0$). The rail vertical mobility does not vary so much near the natural frequency of the wheel. The rail dynamic complex stiffness at the contact point is therefore supposed to be almost constant near the natural frequency of the wheel such that:

$$k^r(0, \omega) \simeq k^r(0, \Omega) \tag{26}$$

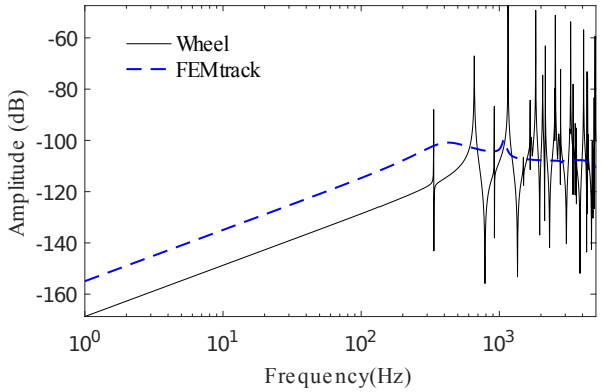

Figure 18: Comparison of rail and wheel vertical mobilities at the contact point (Reference amplitude: 1 m/s/N)

Thus, near the natural frequency of the considered wheel mode, we have: $\eta_c(\omega) \approxeq \eta_c(\Omega)$ and Eq. (22) becomes:

$$\left(-\omega^2 + 2i\omega\xi_c\Omega + \Omega^2 + \text{Real}(K_c)\right) q = 0 \tag{27}$$

where the total damping factor ξ_c is thus given by:

$$\xi_c = \xi^w + \eta_c \tag{28}$$

Eq. (27) gives:

$$\omega = i\xi_c\Omega \pm \sqrt{-\xi_c^2\Omega^2 + \Omega^2 + \text{Real}(K_c)} \tag{29}$$

The unknown generalized coordinate corresponding to the wheel mode q is given by:

$$q = q_o e^{i\omega t} = q_o e^{-\xi_c\Omega t} e^{\pm i\sqrt{-\xi_c^2\Omega^2+\Omega^2+\text{Real}(K_c)}t} \tag{30}$$

where q_o is the amplitude of q.

The unstable frequency is given by:

$$f_{unstable} = \frac{\sqrt{-\xi_c^2\Omega^2 + \Omega^2 + \text{Real}(K_c)}}{2\pi} \tag{31}$$

The divergence rate of the coupled complex mode can be defined using the real and imaginary terms in Eq. (29):

$$DvR = \frac{-\xi_c\Omega}{\sqrt{-\xi_c^2\Omega^2 + \Omega^2 + \text{Real}(K_c)}} \tag{32}$$

Stability criterion

The sign of damping factor ξ_c (Eq. (28)) is the key factor for the stability of the system. If this damping factor is negative, the divergence rate is positive and the wheel/rail system becomes unstable. If the wheel mode damping ξ^w is sufficiently greater than the negative damping η_c, instabilities do not occur.

Looking at Eq. (23), it is clear that this may occur for sufficiently high value of $\mu > |\Phi_z^w/\Phi_y^w|$ in the case where the sign of (s_{y0}) is the same as the sign of the product $\Phi_z\Phi_y$. However a numerical application has to be performed in order to evaluate if this negative damping is sufficient to destabilize the system in realistic cases, i.e. $-\eta_c > \xi^w$.

3.3. Numerical application

In this section, the results of stability analysis of the wheel/rail system for the reference case obtained from the Eqs. (31) and (32) for all wheel modes are firstly presented. The bifurcation curves (effect of friction coefficient) then allow for analysis of the instability mechanism.

3.3.1. Reference case analysis

The reference case with the kinematic parameters listed in Table 3 is considered. A divergent rate in Eq. (32) is calculated for all computed wheel modes using η_c values given by Eq. (25). Results given on Fig. 19 for $s_{y0} > 0$, $k^H = 1260$ MN/m and $\mu = 0.3$ show that only three unstable modes are found ($\xi < 0$) which correspond to the three axial wheel modes without nodal circle (a,0,2), (a,0,3) and (a,0,4), with natural frequencies 334 Hz, 919 Hz and 1670 Hz respectively. The divergent rates corresponding to these three mode are 0.48%, 0.42% and 0.13%. These positive divergent rates traduce the fact that negative damping η_c added by the frictional contact with the rail is greater than the modal damping factor ($\xi = 0.01\%$ for these modes). These unstable modes are the same as the three first modes found in the previous section. Thus, the kind of instabilities in a single wheel mode coupling with the track vertical complex stiffness can be reproduced though an 1-DOF model. As expected for this 1-DOF model, the unstable mode (a,0,6) found in the previous section due to the modes coupling is not found. This result is coherent with the fact that the fundamental frequencies correspond to axial wheel modes with zero nodal circles from literature review [3, 4] and the result of the previous section.

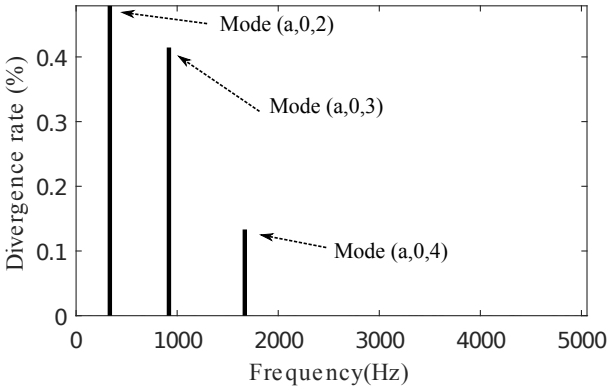

Figure 19: Divergence rates obtained with the 1-DOF model in the reference case

3.3.2. Bifurcation curves

While the other parameters are maintained constant, the bifurcation curves of the unstable modes are presented in Fig. 20. The critical friction coefficient from which the system becomes unstable are respectively 0.06, 0.08, 0.15 for the wheel modes (a,0,2), (a,0,3) and (a,0,4). In comparison with the results of the previous section, the critical friction coefficients for the unstable modes are not so different ($\mu = 0.06$, $\mu = 0.09$ and $\mu = 0.22$ respectively).

Fig. 20 shows the linear evolution of the divergence rate of the unstable modes since the relation between the imaginary part of K_c and μ is linear (Eq. (23)). The results obtained by this model are similar to the results obtained by the FEM model developed in the previous section. Thus, it can be concluded that the imaginary part of the track vertical complex stiffness is responsible for the instabilities of a single wheel mode.

In this section, the mechanism which explains instabilities in a single wheel mode coupling with the track vertical dynamic is clarified by an 1-DOF model. It is found that instability represented by a negative damping is introduced in the system due to the imaginary part of the track vertical complex stiffness. The system becomes unstable if the natural wheel damping is inferior to this negative damping. Obviously, there is no mode coupling when using this model. That is the major difference between this 1-DOF model and the 2-DOF model developed by Ding *et al.* [31].

4. Conclusion

The present works dealt with the problematic of curve squeal of railway systems. The aim was to make a contribution to the study of instability mechanisms leading to curve squeal.

A stability analysis of wheel/rail rolling contact in the case of lateral full sliding was proposed in order to investigate the instability mechanisms. A point contact model with linearized Hertzian normal law and Coulomb's friction law is used in all the parts. The interaction model firstly uses full wheel and rail modal bases. It was found that even with a constant Coulomb friction, instabilities can occur because of the coupling between normal and tangential dynamics in wheel/rail systems. This coupling can involve two wheel modes (mode coupling) or only one wheel mode (among axial modes with 2 to 4 nodal diameters and 0 nodal circle) when the rail dynamics is included. It has been shown that the last case corresponds to a specific and original mechanism. These results are coherent with experimental observations (modal shapes, frequencies, parametric influences, etc.). The rail vertical flexibility is found to play an important role in the instability occurrence without "falling friction" nor without "mode-coupling".

This role has secondly been clarified with a simple model in which the wheel is represented by one mode and the track by a vertical complex stiffness. With this model, it was found that the imaginary part of the complex stiffness of the rail, induced by the phase shift of the propagating wave but also by pad and rail damping plays a critical role in the instability mechanism. The combination of friction and phase shift induces a negative damping, which may then destabilize the system, leading to self-sustained vibration and squeal noise.

In comparison with existing models, this work has given one major originality. A specific mechanism has been found and explained by proposing an appropriate simple 1-DOF model. Results obtained with the simplified model

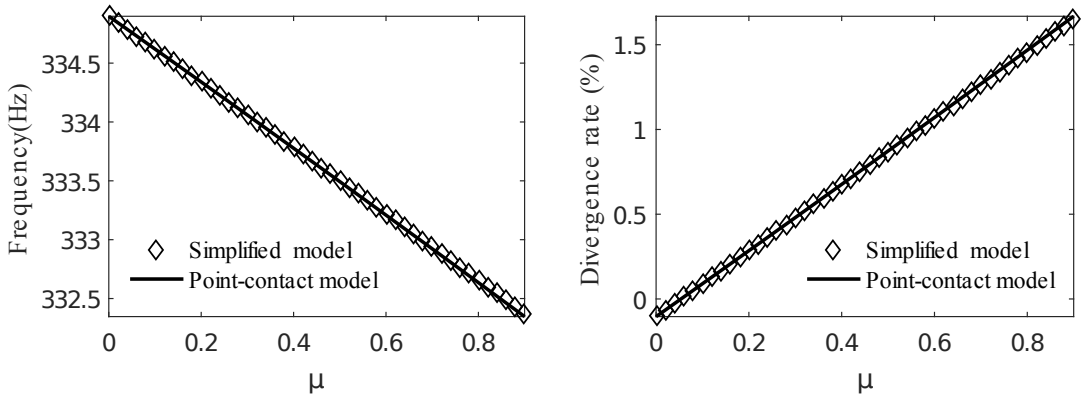

(a) Mode (a,0,2)

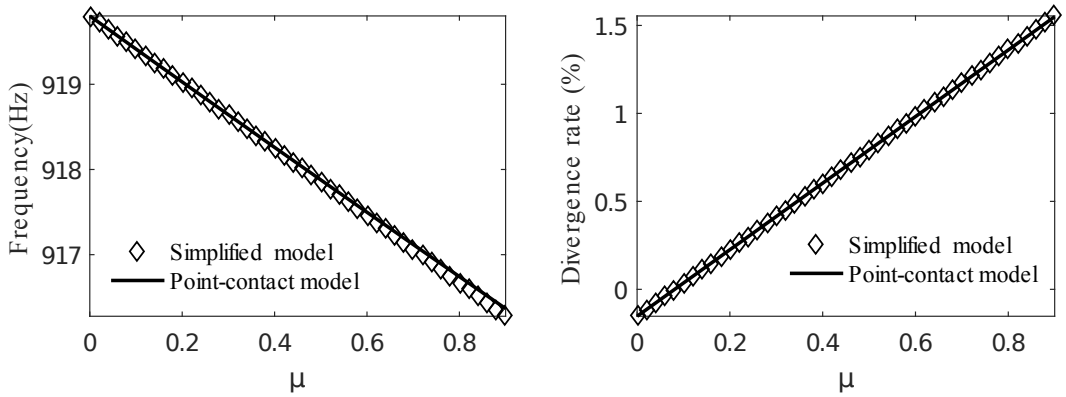

(b) Mode (a,0,3)

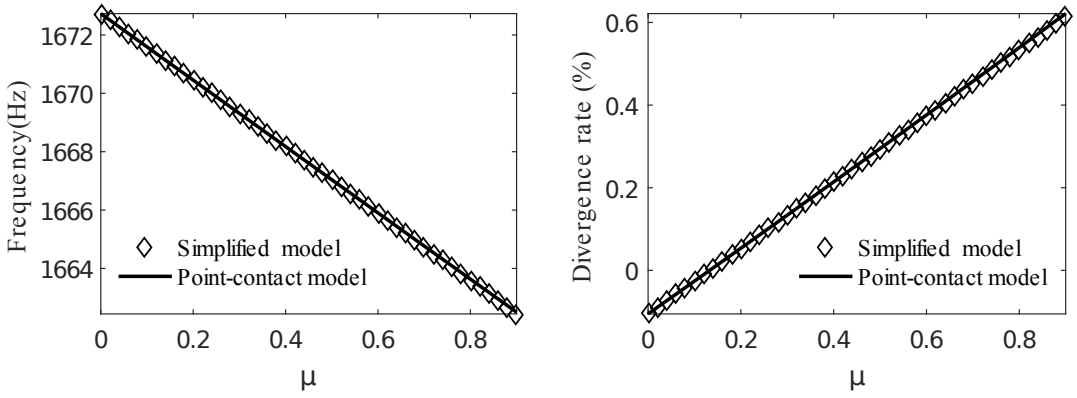

(c) Mode (a,0,4)

Figure 20: Bifurcation curves of the unstable complex modes for the 1-DOF model

show good agreement with those obtained with the finite element model in terms of unstable frequencies. This mechanism shows the crucial role of the track on the stability of wheel/rail system in curve. It opens several mitigation solutions which are not only concentrated on the wheel but also on the track. In addition to the increase of the damping of the wheel (Eq. (28)), to reduce the squeal occurrence, the decrease of the negative damping introduced by the track dynamics can be performed by reducing the friction coefficient at the contact zone, the imaginary part of the equivalent stiffness combining the contact stiffness and the track vertical complex stiffness or the wheel dynamics (Eq. (23)). An important prospect of this work is an experimental validation of the mechanisms highlighted in this work. For the mode coupling mechanism, "simple experiments" can be designed with a two components frictional system (as for example in: Bigoni *et al.* 's experiments [45, 46]). But to validate experimentally the 1-DOF model proposed here, a question that stands out is how to represent a complex stiffness, which introduces a negative damping in the system. It is not simple and needs a new kind of experiment.

Acknowledgement

This work was carried out within the CERVIFER project backed by the ADEME organization and the Haut-de-France region and within the framework of the LABEX CeLyA (ANR-10-LABX-0060) of Universit de Lyon, within the program " Investissements dAvenir " (ANR-11-IDEX-0007) operated by the French National Research Agency (ANR). The authors gratefully acknowledge the support of these institutions.

References

[1] D. Eadie, M. Santoro, Top-of-rail friction control for curve noise mitigation and corrugation rate reduction, Journal of Sound and Vibration 293 (2006) 747–757.
[2] D. T. Eadie, M. Santoro, J. Kalousek, Railway noise and the effect of top of rail liquid friction modifiers: changes in sound and vibration spectral distributions in curves, Wear 258 (7-8) (2005) 1148–1155.
[3] N. Vincent, J. Koch, H. Chollet, J. Guerder, Curve squeal of urban rolling stockpart 1: State of the art and field measurements, Journal of sound and vibration 293 (2006) 691–700.
[4] J. Koch, N. Vincent, H. Chollet, O. Chiello, Curve squeal of urban rolling stockpart 2: Parametric study on a 1/4 scale test rig, Journal of sound and vibration 293 (2006) 701–709.
[5] M. Rudd, Wheel/rail noise-part ii: Wheel squeal, Journal of Sound and Vibration 46 (1976) 381–394.
[6] C. Glocker, E. Cataldi-Spinola, R. Leine, Curve squealing of trains: Measurement, modelling and simulation, Journal of Sound and Vibration 324 (2009) 365–386.
[7] P. Remington, Wheel/rail squeal and impact noise: What do we know? what don't we know? where do we go from here?, Journal of Sound and Vibration 116 (1987) 339–353.
[8] K. Popp, P. Stelter, Stick-slip vibrations and chaos, Philosophical Transactions: Physical Sciences and Engineering (1990) 89–105.
[9] M. Bengisu, A. Akay, Stability of friction-induced vibrations in multi-degree-of-freedom systems, Journal of Sound and Vibration 171 (1994) 557–570.
[10] R. Ibrahim, Friction-induced vibration, chatter, squeal, and chaospart i: Mechanics of contact and friction, Applied Mechanics Reviews 47 (1994) 209–226.
[11] J. Oden, J. Martins, Models and computational methods for dynamic friction phenomena, Computer methods in applied mechanics and engineering 52 (1985) 527–634.
[12] V. Aronov, A. Dsouza, S. Kalpakjian, I. Shareef, Experimental investigation of the effect of system rigidity on wear and friction-induced vibrations, Journal of Lubrication Technology 105 (1983) 206–211.
[13] V. Aronov, A. Dsouza, S. Kalpakjian, I. Shareef, Interactions among friction, wear, and system stiffnesspart 1: effect of normal load and system stiffness, Journal of Tribology 106 (1984) 54–58.
[14] N. Hoffmann, M. Fischer, R. Allgaier, L. Gaul, A minimal model for studying properties of the mode-coupling type instability in friction induced oscillations, Mechanics Research Communications 29 (2002) 197–205.
[15] U. von Wagner, D. Hochlenert, P. Hagedorn, Minimal models for disk brake squeal, Journal of Sound and Vibration 302 (2007) 527–539.
[16] J.-J. Sinou, L. Jezequel, Mode coupling instability in friction-induced vibrations and its dependency on system parameters including damping, European Journal of Mechanics-A/Solids 26 (2007) 106–122.
[17] C. Van Ruiten, Mechanism of squeal noise generated by trams, Journal of Sound and Vibration 120 (1988) 245–253.
[18] E. Schneider, K. Popp, H. Irretier, Noise generation in railway wheels due to rail-wheel contact forces, Journal of Sound and Vibration 120 (1988) 227–244.
[19] U. Fingberg, A model of wheel-rail squealing noise, Journal of Sound and Vibration 143 (1990) 365–377.
[20] F. J. Périard, Wheel-rail noise generation: curve squealing by trams, TU Delft, Delft University of Technology, 1998.
[21] M. A. Heckl, I. Abrahams, Curve squeal of train wheels, part 1: mathematical model for its generation, Journal of Sound and Vibration 229 (2000) 669–693.
[22] M. A. Heckl, Curve squeal of train wheels, part 2: Which wheel modes are prone to squeal?, Journal of Sound and Vibration 229 (2000) 695–707.

[23] O. Chiello, J.-B. Ayasse, N. Vincent, J.-R. Koch, Curve squeal of urban rolling stockpart 3: Theoretical model, Journal of sound and vibration 293 (2006) 710–727.
[24] B. Ding, G. Squicciarini, D. Thompson, Effects of rail dynamics and friction characteristics on curve squeal, in: Journal of Physics: Conference Series, Vol. 744, IOP Publishing, 2016, p. 012146.
[25] F. De Beer, M. Janssens, P. Kooijman, Squeal noise of rail-bound vehicles influenced by lateral contact position, Journal of Sound and Vibration 267 (2003) 497–507.
[26] J.-F. Brunel, P. Dufrénoy, M. Naït, J.-L. Muñoz, F. Demilly, Transient models for curve squeal noise, Journal of sound and vibration 293 (2006) 758–765.
[27] B. Ding, G. Squicciarini, D. Thompson, R. Corradi, An assessment of mode-coupling and falling-friction mechanisms in railway curve squeal through a simplified approach, Journal of Sound and Vibration 423 (2018) 126–140.
[28] A. Pieringer, A numerical investigation of curve squeal in the case of constant wheel/rail friction, Journal of Sound and Vibration 333 (2014) 4295–4313.
[29] I. Zenzerovic, W. Kropp, A. Pieringer, An engineering time-domain model for curve squeal: Tangential point-contact model and green's functions approach, Journal of Sound and Vibration 376 (2016) 149–165.
[30] I. Zenzerovic, W. Kropp, A. Pieringer, Influence of spin creepage and contact angle on curve squeal: A numerical approach, Journal of Sound and Vibration 419 (2018) 268–280.
[31] B. Ding, G. Squicciarini, D. Thompson, Effect of rail dynamics on curve squeal under constant friction conditions, Journal of Sound and Vibration 442 (2019) 183–199.
[32] E. BALMÈS, Structural dynamics toolbox sdt 5.1, for use with matlab.
[33] D. Thompson, Railway noise and vibration: mechanisms, modelling and means of control, Elsevier, 2008.
[34] A. Pieringer, Time-domain modelling of high-frequency wheel/rail interaction [dissertation], Göteborg: Chalmers University of Technology (2011).
[35] C. Van Ruiten, Mechanism of squeal noise generated by trams, Journal of Sound and Vibration 120 (1988) 245–253.
[36] D. Thompson, B. Hemsworth, N. Vincent, Experimental validation of the twins prediction program for rolling noise, part 1: description of the model and method, Journal of sound and vibration 193 (1996) 123–135.
[37] G. Xie, P. Allen, S. D. Iwnicki, A. Alonso, D. J. Thompson, C. J. Jones, Z. Huang, Introduction of falling friction coefficients into curving calculations for studying curve squeal noise, Vehicle system dynamics 44 (2006) 261–271.
[38] S. S. Hsu, Z. Huang, S. D. Iwnicki, D. J. Thompson, C. J. Jones, G. Xie, P. Allen, Experimental and theoretical investigation of railway wheel squeal, Proceedings of the Institution of Mechanical Engineers, Part F: Journal of Rail and Rapid Transit 221 (2007) 59–73.
[39] G. Squicciarini, S. Usberti, D. Thompson, R. Corradi, A. Barbera, Curve squeal in the presence of two wheel/rail contact points, in: Noise and Vibration Mitigation for Rail Transportation Systems, Springer, 2015, pp. 603–610.
[40] L. Gry, Dynamic modelling of railway track based on wave propagation, Journal of sound and vibration 195 (1996) 477–505.
[41] C.-M. Nilsson, C. Jones, D. Thompson, J. Ryue, A waveguide finite element and boundary element approach to calculating the sound radiated by railway and tram rails, Journal of Sound and Vibration 321 (2009) 813–836.
[42] B. Betgen, G. Squicciarini, D. J. Thompson, On the prediction of rail cross mobility and track decay rates using finite element models, in: Proceedings of the In Proceedings of the 10th European Congress and Exposition on Noise Control Engineering, 2015, p. 2019.
[43] J.-F. Hamet, Railway noise: use of the timoshenko model in rail vibration studies, Acta Acustica united with Acustica 85 (1999) 54–62.
[44] D. Brizard, O. Chiello, J.-J. Sinou, X. Lorang, Performances of some reduced bases for the stability analysis of a disc/pads system in sliding contact, Journal of Sound and Vibration 330 (2011) 703–720.
[45] D. Bigoni, G. Noselli, Experimental evidence of flutter and divergence instabilities induced by dry friction, Journal of the Mechanics and Physics of Solids 59 (10) (2011) 2208–2226.
[46] D. Bigoni, D. Misseroni, G. Noselli, D. Zaccaria, Surprising instabilities of simple elastic structures, Nonlinear Physical Systems: Spectral Analysis, Stability and Bifurcations (2013) 1–14.

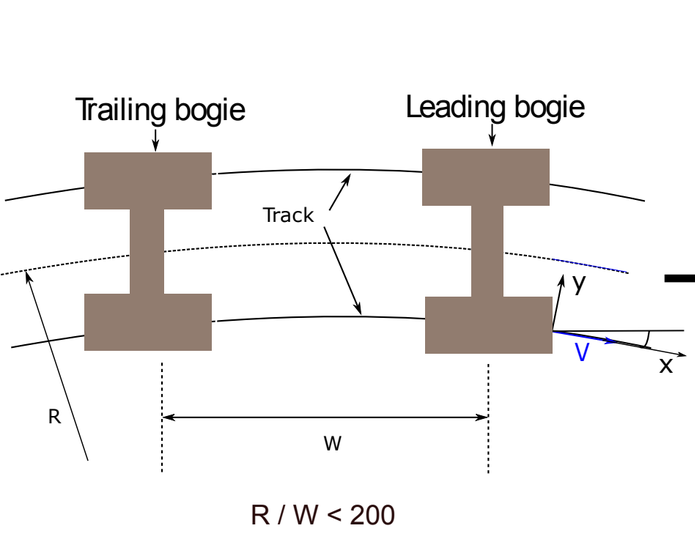

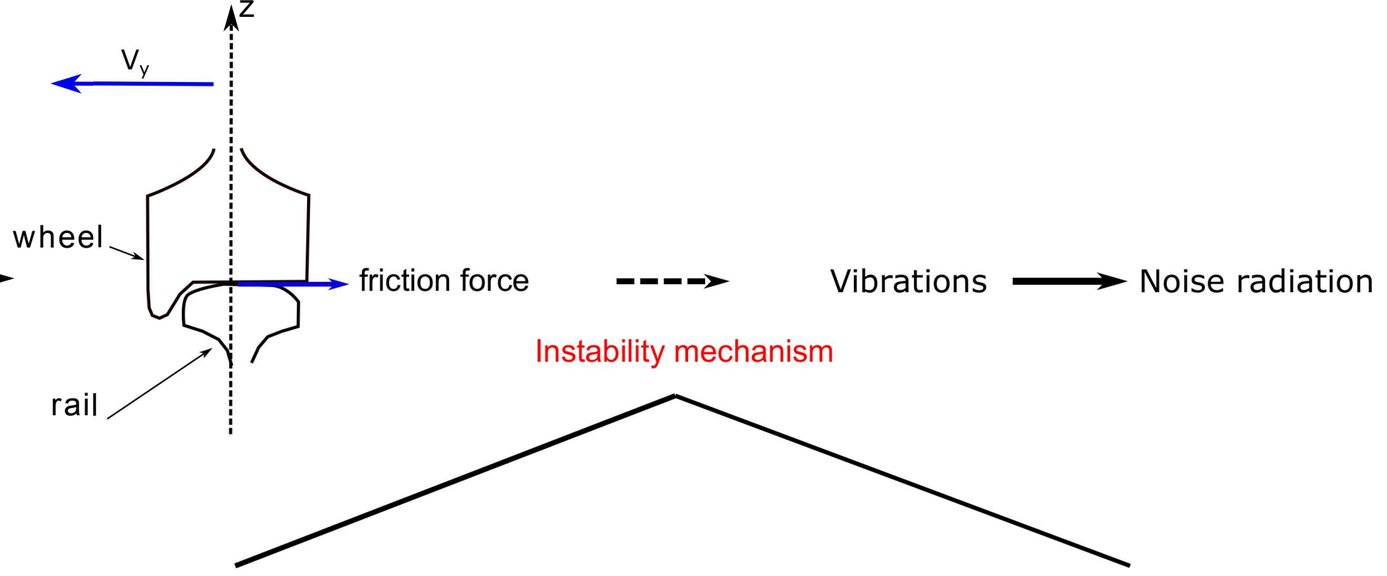

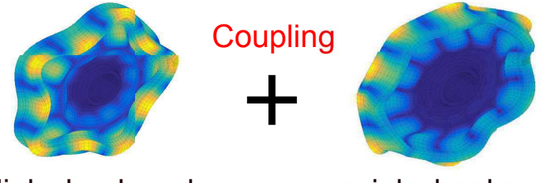

radial wheel mode

axial wheel mode

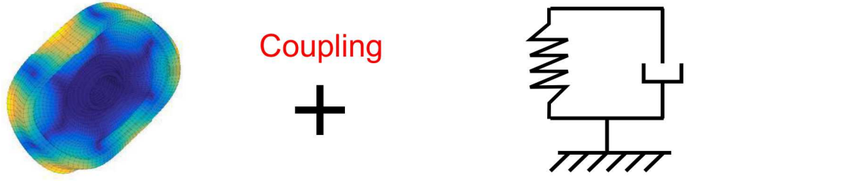

a single wheel mode

track equivalent complex stiffness